ELSEVIER

Earth and Planetary Science Letters 201 (2002) 491–507

EPSL

www.elsevier.com/locate/epsl

Influence of melt on the creep behavior of olivine–basalt aggregates under hydrous conditions

S. Mei [a], W. Bai [b], T. Hiraga [c], D.L. Kohlstedt [c,*]

[a] *Department of Chemical Engineering and Materials Science, University of Minnesota, Minneapolis, MN 55455, USA*
[b] *Department of Geodynamics, Institute of Geophysics, Academia Sinica, Beijing 100101, PR China*
[c] *Department of Geology and Geophysics, University of Minnesota, Minneapolis, MN 55455, USA*

Received 15 October 2001; received in revised form 22 May 2002; accepted 23 May 2002

Abstract

The influence of melt on the creep behavior of olivine–basalt aggregates under hydrous conditions has been investigated by performing a series of high-temperature triaxial compression experiments. Samples with melt fractions of $0.02 \leq \phi \leq 0.12$ were deformed under water-saturated conditions at temperatures between 1373 and 1473 K and a confining pressure of 300 MPa in a gas-medium apparatus. At constant differential stress and temperature, the rate of deformation increased rapidly but systematically with increasing melt fraction. In the diffusion creep regime, at a given differential stress, samples with melt fractions of 0.02 and 0.12 deformed a factor of ~ 2 and ~ 20, respectively, faster than a melt-free sample. In the dislocation creep regime, a sample with a melt fraction of 0.12 deformed a factor of ~ 40 faster than a melt-free sample. For partially molten olivine–basalt aggregates deformed under hydrous conditions, the dependence of creep rate on melt fraction can be expressed in the form $\dot{\varepsilon}(\phi) = \dot{\varepsilon}(0) \exp(\alpha\phi)$, where $\alpha \approx 26$ for diffusion creep and $\alpha \approx 31$ for dislocation creep. The results of this study, combined with reasonable estimates for the spatial variation in the concentrations of water and melt (as well as for the geotherm and the activation volume for creep), provide constraints on the viscosity structure of Earth's upper mantle. As an example, we present a viscosity profile for the mantle wedge above a subducting plate, demonstrating that the viscosity in that region can vary by ~ 3 orders of magnitude over a depth of ~ 60 km due to the combined effects of water and melt weakening.

Keywords: creep; viscosity; melts; water; olivine

1. Introduction

The high-temperature creep behavior of olivine-rich rocks directly influences geodynamic processes occurring within Earth's mantle. In many regions of the asthenosphere, such as beneath a mid-ocean ridge or in the mantle wedge above a subducting slab, mantle rocks are thought to be partially or fully saturated with water [1,2]. Furthermore, mantle rocks in these regions may also be partially molten [3,4]. To model convection in such regions, the influence of both melt and water on the creep behavior of olivine-rich rocks must be quantified.

Over the past few decades, systematic laborato-

* Corresponding author. Tel.: +1-612-626-1544; Fax: +1-612-625-3819.
E-mail address: dlkohl@umn.edu (D.L. Kohlstedt).

0012-821X/02/$ – see front matter
PII: S0012-821X(02)00745-8

ry studies have demonstrated that both a small amount of water (i.e. water-related species detected as O–H stretching bands in infrared spectra) and a small amount of melt each reduce the high-temperature creep strength of mantle rocks. In the former case, the high-temperature viscosity of olivine single crystals, melt-free olivine-rich rocks and synthetic olivine-bearing aggregates decreases by a factor of $\sim$5–10 if a trace amount of water is added to an initially dry sample [5–10]. In the latter case, the viscosity of dry olivine aggregates with 5 vol% basalt is a factor of $\sim$5 lower than that of melt-free samples [11–15]. However, to date, no experiments have been conducted on samples containing well-controlled amounts of both melt and water.

Based on the observation that the partition coefficient for hydroxyl ions between olivine and basalt is as large as 10^4 [16,17], Karato [18] proposed that, if the source of water is limited, the strength of a partially molten peridotite may actually be greater than that of a melt-free rock because water would partition preferentially into the melt phase, thereby dehydrating the mineral grains. However, if a partially molten rock is either water-saturated or has access to enough water so that the concentration in the grains exceeds on the order of a hundred atomic parts per million, as likely occurs in a mantle wedge, water and melt should both act to reduce the strength of the rock.

The purpose of this paper is to quantify the combined effects of water and melt on the creep behavior of olivine aggregates. As indicated above, some regions in the mantle are likely to be both partially molten and water-rich. In this case, the combined weakening effects of water and melt must be taken into account in order to understand the dynamic behavior of such regions. To achieve this goal, olivine–basalt aggregates were deformed under water-saturated conditions. Establishing a water-saturated condition for experiments is important for two reasons. First, for conducting experiments under hydrous conditions with a defined thermodynamic state, water concentration (or water fugacity) must be well-controlled. A water-saturated condition is ideal for meeting this requirement. Second, to compare creep results for samples with different melt fractions deformed under hydrous conditions, all the samples should have the same concentration of water. This situation can be readily achieved at water-saturated conditions for experiments carried out at a given pressure, temperature and oxygen fugacity.

2. Experimental details

2.1. Sample preparation and assembly

Samples for deformation experiments were fabricated from powdered San Carlos olivine and powdered mid-ocean ridge basalt (MORB) [19]. Olivine powder with a particle size of $\sim$10 μm was mixed mechanically with 1, 4 or 7 wt% MORB with a particle size of $<$8 μm. The mixed powders were tumbled in a sealed polyethylene jar and then stirred in a water slurry for 24 h using a teflon-coated magnetic stirrer. After this mixing step, water was removed by evaporation, and the powders were stored in a vacuum oven at 415 K. The powders were then cold-pressed into a nickel capsule under a uniaxial pressure of 200 MPa and subsequently isostatically hot-pressed at 1523 K and 300 MPa for 3–4 h in a gas-medium apparatus. The oxygen fugacity during hot-pressing was buffered near Ni–NiO by oxidation of the nickel capsule. After hot-pressing, the nickel capsule was dissolved using aqua regia (a mixture of nitric acid and hydrochloric acid). For the deformation experiments, cylindrical specimens 7.0 mm in diameter and $\sim$14.5 mm in length were fashioned from the hot-pressed cylinders with a diamond coring drill. The ends of sample were polished to be flat and parallel to within a few μm.

Deformation experiments were mainly conducted under hydrous conditions. Samples were wrapped in 0.12 mm thick nickel foil and inserted into a talc sleeve 14 mm long, 7.5 mm in inner diameter and 9.8 mm in outer diameter. This sample assembly was then welded into a nickel capsule. During deformation, oxygen fugacity was buffered near Ni–NiO by oxidation of the surfaces of the Ni foil and the inner wall of the Ni capsule as evidenced by thin, greenish oxide layers at

these locations. Dehydration of the talc near 1070 K provided a source (~60 mg) of water. A more detailed description of the techniques used to fabricate samples and to prepare sample assemblies was presented by Mei and Kohlstedt [9,10].

2.2. Deformation experiments

Samples were deformed under constant load conditions in a gas-medium apparatus [20] at a confining pressure of 300 MPa and temperatures between 1373 and 1473 K. In calibration tests, the temperature variation along the length of a sample was ~2 K. In a deformation test with a thermocouple in contact with the upper end of the sample assembly, we estimate that the uncertainty in temperature along the length of the sample is ≲5 K. Reported values for confining pressure are accurate to ±2 MPa.

Creep data were obtained by varying the stress in a stepwise fashion at constant temperature and pressure or by varying temperature at constant stress and pressure. For most samples, a constant strain rate was achieved by about 1% strain. At the end of each experiment, the sample was cooled under load at a rate of ~2 K/s to 900 K. The load was then removed and the sample was brought to ambient conditions at a cooling rate of ~1 K/s and a depressurization rate of 1–2 MPa/s.

2.3. Analysis techniques

2.3.1. Infrared analysis

Water concentrations within deformed samples were determined by Fourier transform infrared (FTIR) spectroscopy. In some cases, an oriented olivine single crystal was placed within the sample for evaluating the water concentration within olivine grains. Infrared spectra in the wavenumber ranging from 2000 to 4000 cm^{-1} were collected with a micro-FTIR spectrometer with a wavelength resolution of better than 1 cm^{-1}. Room-temperature absorption spectra were obtained on doubly polished sections of ~100 μm thickness.

After making a background correction using a third-order polynomial fit to the background absorbance, the hydroxyl concentration was calculated from infrared spectra by integrating across the hydroxyl bands. Specifically, hydroxyl concentration was determined from the relation [21]:

$$C_{OH} = \frac{1}{150\gamma} \int \frac{K(\nu)}{3780-\nu}\, d\nu \quad (1)$$

where C_{OH} is molar hydroxyl concentration, $K(\nu)$ is the absorption coefficient (in cm^{-1}) at wavenumber ν (in cm^{-1}), and γ is an orientation factor accounting for the orientation distribution of the OH groups. For the isotropic broad absorption bands obtained from polycrystalline samples, a value of $\gamma = 1/3$ was used; for the anisotropic, sharp bands obtained from single crystals with unpolarized radiation and the infrared beam direction parallel to the *b*-axis of olivine, a value of $\gamma = 1/2$ was used [21].

2.3.2. Analysis of creep data

Stress and strain rate versus time were calculated from the recorded load and displacement versus time data, respectively. Values of stress were corrected for the strengths of the Fe jacket, Ni sleeve and talc (i.e. a mixture of enstatite, quartz and water at run conditions) sleeve as well as for the change in sample cross section during deformation. The creep strengths of Fe and Ni were taken from Frost and Ashby [22], and those for talc were determined as part of this study (see Table 1). The Fe, Ni and talc supported about 10% of the total applied load.

The deformation results were analyzed in terms of a power-law creep equation of the form:

$$\dot{\varepsilon}(\sigma,\ d,\ \phi,\ C_{OH},\ T,\ P) = A\frac{\sigma^n}{d^m} f(\phi,\ C_{OH}) \exp\left(-\frac{Q+PV^*}{RT}\right) \quad (2)$$

where $\dot{\varepsilon}$ is the axial strain rate, σ the applied differential stress, d the grain size, A a material's parameter, ϕ the melt fraction, Q the activation energy for creep, P the confining pressure, and V^* the activation volume for creep; RT has the usual meaning. For olivine aggregates deformed under hydrous conditions, $n \approx 3.5$ and $m = 0$ in the dislocation creep while $n \approx 1$, $m \approx 3$ in the diffusion

Table 1
Experimental conditions and creep results

Experiment number	ϕ	T (K)	d_0 (μm)	σ (MPa)	$\dot{\varepsilon}$ (s^{-1})
PI-414	0.075	1373	12.6	44	1.3×10^{-5}
				94	3.0×10^{-5}
				119	4.5×10^{-5}
				153	7.8×10^{-5}
		1473		112	2.9×10^{-4}
				85	1.8×10^{-4}
				71	1.1×10^{-4}
				47	6.4×10^{-5}
				39	5.7×10^{-5}
				29	4.5×10^{-5}
PI-417	0.115	1373	13.5	53	2.5×10^{-5}
				85	5.8×10^{-5}
				110	8.4×10^{-5}
				144	1.6×10^{-4}
				179	2.4×10^{-4}
				55	2.3×10^{-5}
		1423		86	2.1×10^{-4}
				53	1.1×10^{-4}
				41	8.5×10^{-4}
				108	3.2×10^{-4}
PI-423	0.021	1373	11.2	19	1.8×10^{-6}
				42	2.7×10^{-6}
				63	3.4×10^{-6}
				84	5.0×10^{-6}
				107	8.3×10^{-6}
				126	1.3×10^{-5}
				147	1.8×10^{-5}
				167	2.4×10^{-5}
				197	3.6×10^{-5}
		1423		19	3.7×10^{-6}
				39	6.5×10^{-6}
				62	1.2×10^{-5}
				83	1.7×10^{-5}
				105	2.4×10^{-5}
				120	2.9×10^{-5}
				165	6.1×10^{-5}
		1473		61	2.7×10^{-5}
				99	5.4×10^{-5}
				158	1.3×10^{-4}
				40	1.4×10^{-4}
PI-436	0.08	1423	11.8	41	2.9×10^{-5}
				94	9.2×10^{-5}
PI-446	0.085	1423	10.6	64	3.8×10^{-5}
				88	7.6×10^{-5}
				37	2.22×10^{-5}
				63	4.0×10^{-5}
				39	2.1×10^{-5}
				89	7.1×10^{-5}
				140	1.7×10^{-4}
				114	1.1×10^{-4}

Table 1 (*Continued*).

Experiment number	ϕ	T (K)	d_0 (μm)	σ (MPa)	$\dot{\varepsilon}$ (s^{-1})
PI-449	0.083	1473	10.3	46	1.0×10^{-4}
				72	1.4×10^{-4}
				99	2.4×10^{-4}
				48	7.2×10^{-5}
				36	5.2×10^{-5}
				51	7.3×10^{-5}
				29	3.3×10^{-5}
PI-454	0.125	1423	9.8	46	1.1×10^{-4}
				81	2.2×10^{-4}
				46	9.9×10^{-5}
				29	4.6×10^{-5}
				15	2.6×10^{-5}
				61	1.5×10^{-4}
PI-456	0.12	1473	12.3	73	3.2×10^{-4}
				46	1.5×10^{-4}
				35	1.1×10^{-4}
				73	3.5×10^{-4}
				22	7.1×10^{-4}
				57	2.1×10^{-4}
PI-459	0.023	1423	10.1	40	8.9×10^{-6}
				65	1.5×10^{-5}
				98	2.5×10^{-5}
				151	3.6×10^{-5}
PI-461	0.025	1473	13.2	51	1.6×10^{-5}
				78	2.9×10^{-5}
				106	4.4×10^{-5}
				132	7.0×10^{-5}
				107	3.6×10^{-5}
				160	9.2×10^{-5}
Talc		1323	–	7	1.1×10^{-5}
				10	6.3×10^{-5}
				15	9.9×10^{-5}
				11	8.1×10^{-5}

creep regime [9,10]. For olivine–basalt aggregates deformed under anhydrous conditions, similar values were obtained for n and m [14,15].

2.3.3. *Analysis of microstructures and compositions*

The microstructures of deformed samples were analyzed using optical microscopy, scanning electron microscopy (SEM), and transmission electron microscopy (TEM). Apparent dihedral angles were determined from a statistical analysis of more than 100 measurements of triple junctions on SEM and TEM micrographs. Melt fraction was calculated from binary images of digital optical micrographs, and grain sizes were determined using the line-intercept method with a correction factor of 1.5 [23].

3. Experimental results

Experimental results including mechanical data, such as stress and strain rate, as well as sample parameters, such as grain size and melt fraction, are presented in Table 1.

3.1. *Mechanical data*

Results from creep tests conducted under hydrous conditions suggest a transition from defor-

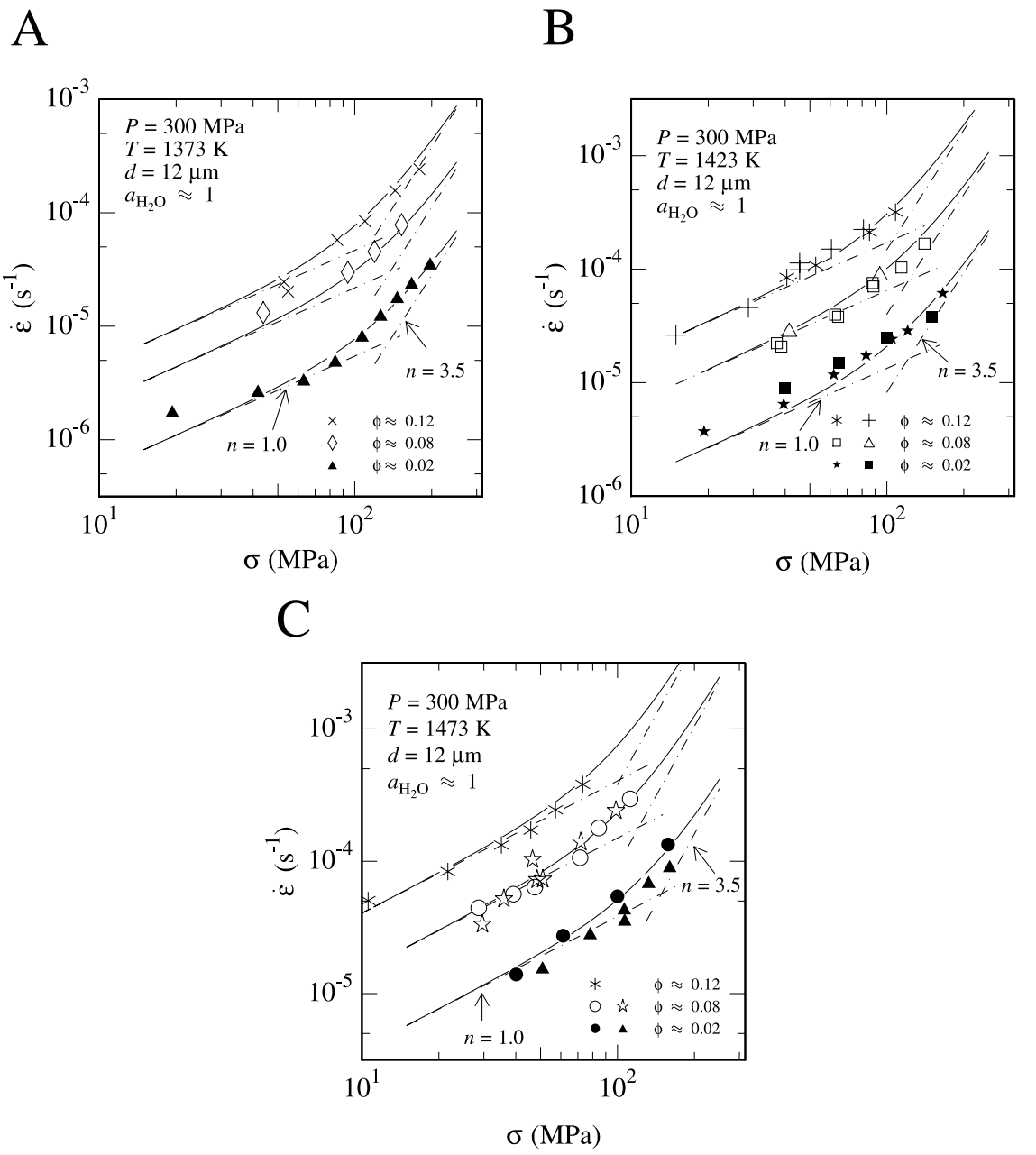

Fig. 1. Log–log plot of strain rate versus stress for samples with different melt fractions deformed at different temperatures. The solid curves are non-linear least-squares fits to the data using a constitutive equation composed of two power-law creep equations. The individual power-law equations are shown by dashed straight lines. (A) Samples deformed at 1373 K with melt fractions of 0.02 (PI-423: solid triangles), 0.08 (PI-414: open diamonds), and 0.12 (PI-417: crosses). (B) Samples deformed at 1423 K with melt fractions of 0.02 (PI-423: solid stars; PI-459: solid squares), 0.08 (PI-436: open triangles; PI-446: open squares), and 0.12 (PI-417: pluses; PI-454: asterisks). (C) Samples deformed at 1473 K with melt fractions of 0.02 (PI-423: solid circles; PI-461: solid triangles), 0.08 (PI-414: open circles; PI-449: open stars), and 0.12 (PI-456: asterisks).

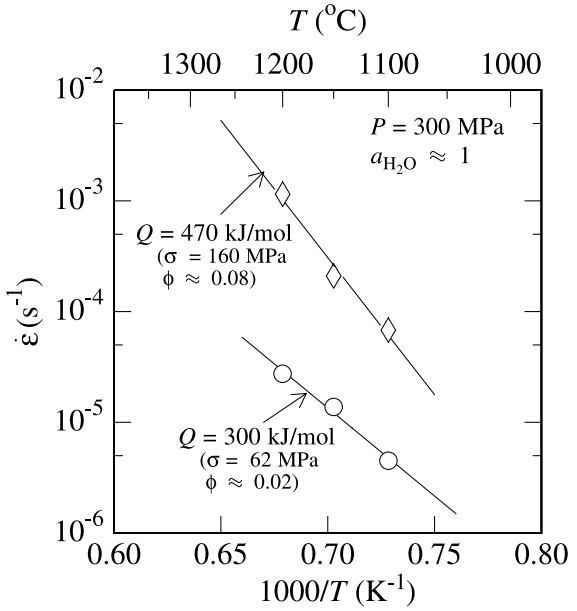

Fig. 2. Arrhenius plot of strain rate versus inverse temperature for both the diffusion and the dislocation creep regimes. Diffusion creep data (open circles) are from sample PI-423. Dislocation creep data (open diamonds) are average values from Fig. 1 at a differential stress of 160 MPa.

mation dominated by diffusion creep at lower differential stresses to deformation dominated by dislocation creep at higher differential stresses. The transition between the two regimes is illustrated in the log–log plots of stress versus strain rate in Fig. 1A–C for samples with melt fractions of 0.02, 0.08 and 0.12 deformed at 1373, 1423 and 1473 K, respectively. The data were fit to a constitutive equation constructed from the sum of two power-law relationships of the form given in Eq. 2 using a non-linear least-squares fitting algorithm with the diffusion creep stress exponent fixed at unity, consistent with the value obtained in previous studies [9,14]. For the experimental conditions investigated in this study, the differential stress at the transition from diffusion creep to dislocation creep increases from ~100 to ~140 MPa as the melt fraction is decreased from 0.12 to 0.02.

3.1.1. Activation energy for creep of partially molten samples under hydrous conditions

Experiments were conducted to constrain the activation energy for the creep of olivine–basalt aggregates under hydrous conditions. The Arrhenius plot in Fig. 2 illustrates the effect of temperature on strain rate for an experiment (PI-423) in which a sample with 2 vol% melt was deformed in the diffusion creep regime at a confining pressure of 300 MPa and a differential stress of 62 MPa. The liquidus for wet basalt is ~1373 K, and the melt fraction in these experiments is approximately constant [24]. A linear least-squares fit of the data yields $Q = 300 \pm 40$ kJ/mol.

In the dislocation creep regime, however, no experiment was conducted at more than one temperature. Therefore, the activation energy was determined from the creep data for a group of samples with the same melt fraction each of which was deformed at a single temperature. The Arrhenius plot in Fig. 2 also illustrates the effect of temperature on strain rate in the dislocation creep regime. Data points are average values taken from Fig. 1 at a differential stress of 160 MPa. These data yield an activation energy of $Q = 470 \pm 50$ kJ/mol.

3.2. Water content of deformed samples

FTIR spectra from olivine single crystals embedded in polycrystalline samples that were deformed under hydrous conditions are presented in Fig. 3A as absorption coefficient versus wavenumber. The hydroxyl concentration in two crystals, one from a sample with $\phi = 0.02$ and the other from a sample with $\phi = 0.12$, is 220 ± 30 H/10^6 Si. Based on published results for water solubility in olivine as a function of water fugacity and confining pressure [25,26], we conclude that our samples were saturated with water.

To quantify the amount of water in our deformed olivine–basalt aggregates, infrared spectra from three samples are presented in Fig. 3B. The concentration of hydroxyl increases from 1.1×10^4 to 4.1×10^4 to 5.3×10^4 H/10^6Si as melt fraction is increased from 0.02 to 0.08 to 0.12, respectively. In the partially molten samples, water is present within the olivine grains, along the grain boundaries, and within the melt phase. Hence, the concentration of water in an olivine–basalt aggregate ($C_{OH}^{ol+melt}$) can be expressed in terms of the concen-

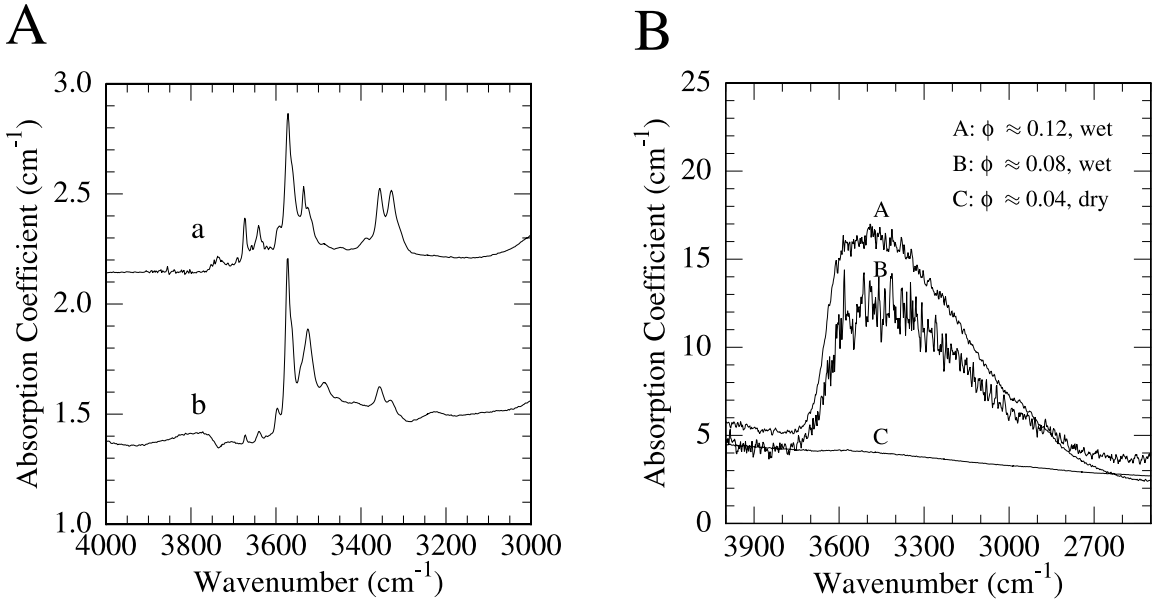

Fig. 3. Infrared absorption spectra obtained on experimentally deformed samples. (A) Spectra from single crystals of olivine embedded in polycrystalline samples. Spectra a and b are from samples PI-454 ($\phi = 0.12$) and PI-461 ($\phi = 0.02$). (B) Spectra from polycrystalline samples. Spectra A, B and C are from samples PI-454, PI-446 and PI-434.

tration of water in the olivine grains and grain boundaries (C_{OH}^{ol}) combined with the concentration in the melt phase (C_{OH}^{melt}) as:

$$C_{OH}^{ol+melt} = (1-\phi)C_{OH}^{ol} + \phi C_{OH}^{melt} = C_{OH}^{ol} + \phi(C_{OH}^{melt} - C_{OH}^{ol}) \quad (3)$$

Water concentration in the olivine–basalt aggregates is plotted versus melt fraction in Fig. 4. A least-squares fit of the above equation to the data yields $C_{OH}^{ol} \approx 4.1 \times 10^3$ H/10^{6}Si and $C_{OH}^{melt} - C_{OH}^{ol} \approx 3.7 \times 10^5$ H/10^{6}Si, respectively. These values are in good agreement with those published for melt-free olivine aggregates [9] and for silicate glasses [27], respectively, for conditions similar to those used in our experiments. Since the OH concentration in the olivine grains is $\sim 0.2 \times 10^3$ H/10^{6}Si, most of the hydroxyl in the olivine aggregates must reside in the grain boundaries, and the partition coefficient for OH between the olivine grains and the melt is $\sim 5 \times 10^{-4}$.

3.3. Distribution of melt under hydrous conditions

Examples of the microstructures of our partially molten samples deformed under hydrous conditions are presented in Fig. 5A–C for melt fractions of 0.02, 0.08 and 0.12. Melt is present in triple junctions and along some grain boundaries. This observation agrees with observations made

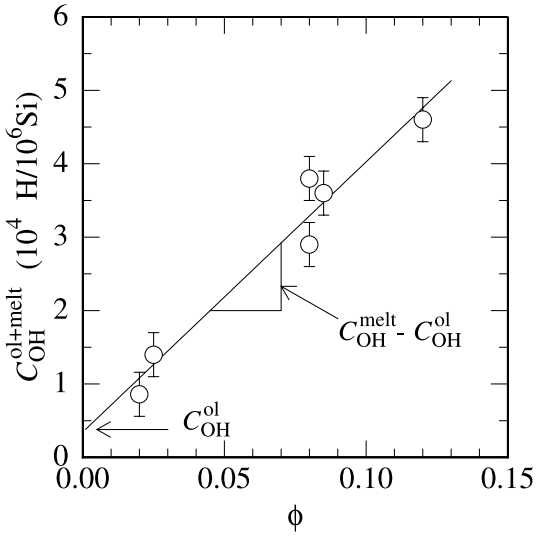

Fig. 4. Total OH concentration versus melt fraction for deformed olivine–basalt aggregates.

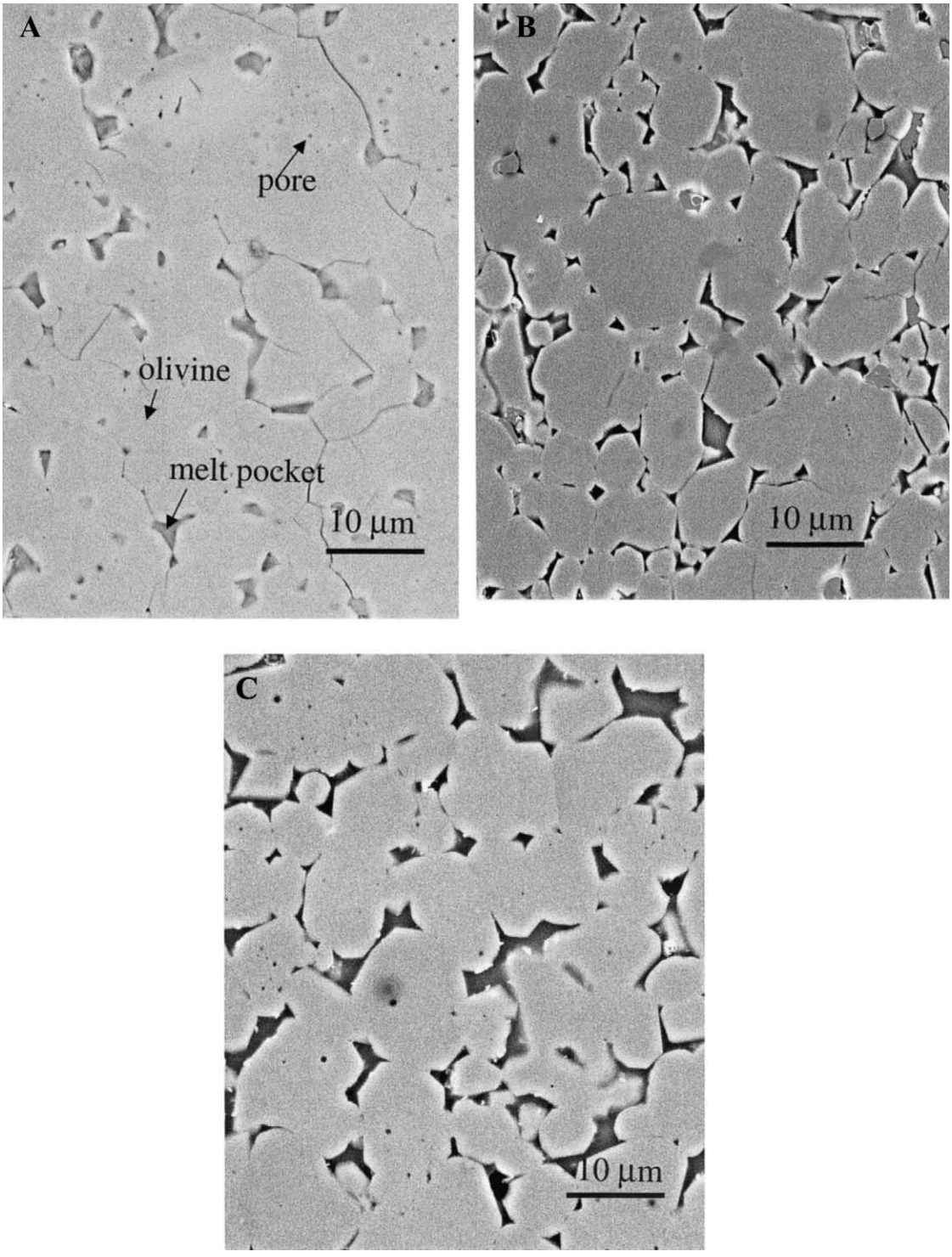

Fig. 5. SEM micrographs of deformed samples with (A) $\phi = 0.02$, (B) $\phi = 0.08$ and (C) $\phi = 0.12$.

in several previous studies of interconnectivity of melt in ultramafic rocks [28,29] as well as in studies of deformation of partially molten olivine–basalt aggregates under anhydrous conditions [14]. Melt topology is further illustrated with the TEM micrographs presented in Fig. 6. Examples of melt-filled triple junctions and of a wetted grain boundary connecting two melt-filled triple junctions are presented in Fig. 6A,B, respectively. The fraction of the grain boundaries wetted by melt increases with increasing melt fraction with a marked preference for wetting low-index crystallographic planes [30]. For example, about 38% of the grain boundaries were wetted in the sample with 12 vol% melt, while only 10% of the grain boundaries were wetted in the sample with 2 vol% melt. The increase in the fraction of two-grain boundaries completely wetted by melt, β, with increasing melt fraction is shown in Fig. 7. A linear least-squares fit of the data yields a slope of $\gamma \approx 3$, where the fraction of two-grain boundaries completely wetted by melt is expressed as $\beta = \gamma\phi$. This value is somewhat smaller than that obtained from Hirth and Kohlstedt [14] for aggregates of olivine plus natural basalt deformed under anhydrous conditions. From their data, the fraction of two-grain boundaries completely wetted by melt is $\beta = 4\phi$ (excluding the data obtained on samples of olivine plus synthetic basalt from their fit).

Dihedral angles were measured on TEM micrographs; the resulting distribution of dihedral angles for sample PI-456 is shown in Fig. 8. The mean dihedral angle determined for three samples (PI-449, PI-456 and PI-461) is $28 \pm 3°$. This value is somewhat smaller than those of 30–40° reported for samples prepared under anhydrous conditions as determined from optical and SEM micrographs [31]. The difference between the values of dihedral angle reported for anhydrous and hydrous samples reflects, at least in part, the different measurement techniques; as the resolution of the observation increases (i.e. in going from SEM to TEM observations), the value determined for the dihedral angle tends to decrease. Hence, the morphology of the melt and the dihedral an-

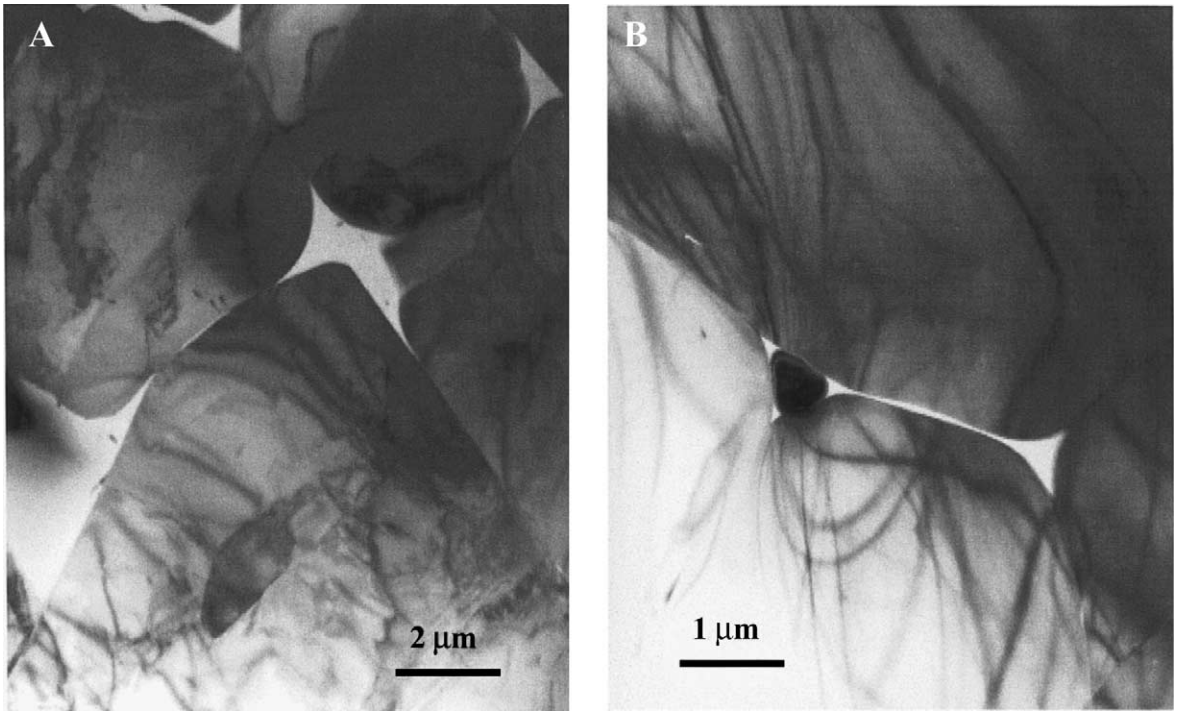

Fig. 6. Dark-field TEM micrographs of deformed samples illustrating (A) melt pockets at triple junctions and (B) grain boundary wetted by melt.

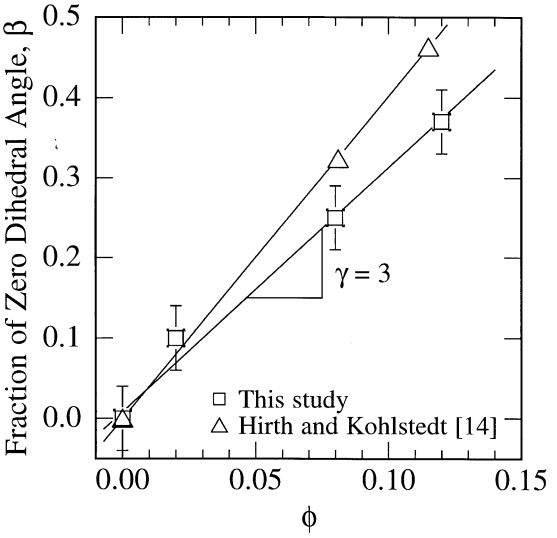

Fig. 7. Fraction of wetted grain boundaries versus melt fraction for samples deformed under water-saturated conditions.

gle in samples exposed to a hydrous environment may not be significantly different from those in samples prepared in an anhydrous environment, if observations of the melt topology are made using a single microscopic technique. This point is supported by the observation of Riley and Kohlstedt [32], who used SEM micrographs to measure dihedral angles for samples of olivine plus melt prepared under both anhydrous and hydrous conditions. These authors demonstrated that the dihedral angles formed under water-absent and water-present conditions in olivine–melt aggregates are equal to within 0.5°.

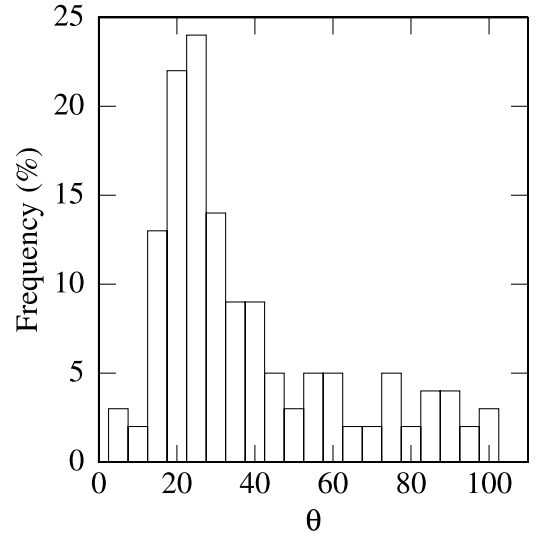

Fig. 8. Measured values of dihedral angle for a deformed sample with a melt fraction of 0.12 (PI-456).

4. Discussion

4.1. Influence of melt fraction on the rheology of olivine–basalt aggregates

At constant differential stress and temperature, the creep rate of olivine–basalt aggregates increases rapidly with increasing melt fraction. As illustrated in Fig. 1, at the same flow stress and temperature, the rate of deformation of olivine–basalt aggregates with a melt fraction of 0.08 is $\sim$5 times faster than the rate of deformation of samples with a melt fraction of 0.02 in the diffusion creep regime and $\sim$7 times faster in the dislocation creep regime.

Creep rate is plotted versus melt fraction for our olivine–basalt aggregates on semi-ln axes in Fig. 9. Data for melt-free samples were taken from Mei and Kohlstedt [9,10]. A linear least-squares fit of the data to an equation describing an exponential dependence of creep rate on melt fraction, $\dot{\varepsilon}(\phi)$, of the form:

$$\dot{\varepsilon}(\phi) = \dot{\varepsilon}(0)\exp(\alpha\phi) \quad (4)$$

yields $\alpha \approx 26$ and 31 for the diffusion creep regime and the dislocation creep regime, respectively, where $\dot{\varepsilon}(0)$ is the strain rate when $\phi = 0$. Kelemen et al. [33] first noted that published data on strain rate versus melt fraction for experiments carried out under anhydrous conditions could be described by the exponential relationship given in Eq. 4; they expressed their conclusion in terms of viscosity, η, as $\eta(\phi) = \eta(0)\exp(-\alpha\phi)$ with a single value of $\alpha = 45$. This value for α is larger than the values determined in our experiments, probably because their analysis was carried out on a large number of data sets composed of results obtained in both the diffusion and the dislocation creep regimes.

An explanation for the physical processes re-

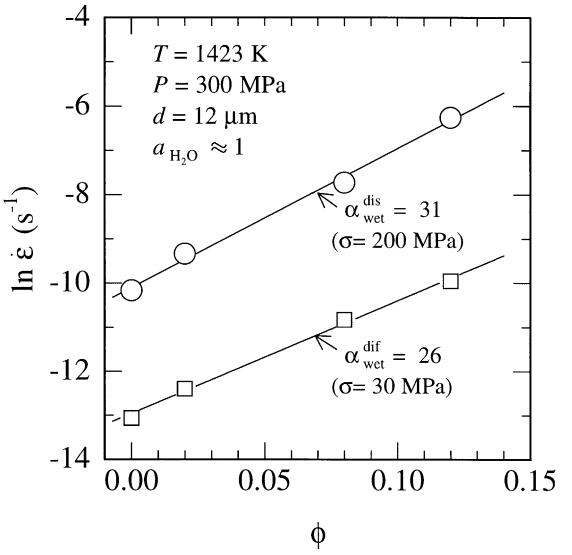

Fig. 9. Strain rate versus melt fraction for samples deformed in the diffusion and dislocation creep regimes under hydrous conditions. Data at $\phi=0$ are from [9,10].

sponsible for the strain rate enhancement has been proposed to explain the dependence of creep rate on melt fraction. Physically, the influence of the liquid basalt phase on the creep rate of olivine–basalt aggregates is two-fold: first, the presence of melt increases the local stress, and second, it enhances the rate of mass transport. These effects have been described by Cooper and Kohlstedt and Cooper et al. [34,35] to account for the influence of melt on deformation rate in the Coble creep regime [36] and is referred to as the CK model below. The CK model is based on the melt distribution in a material with isotropic interfacial energies such that all of the melt is in three- and four-grain junctions, that is, with a dihedral angle (θ) between 0 and 60°. Their analysis yields the following relation between strain rate and melt fraction:

$$\dot{\varepsilon}(\phi)\propto\dot{\varepsilon}(0)\left(1-\frac{\Delta d}{d}\right)^{-2}_{\text{stress}}\left(1-\frac{\Delta d}{d}\right)^{-2}_{\text{diffusion}} \tag{5}$$

where d is a characteristic grain boundary diffusion distance and Δd is the portion of this distance removed due to the presence of melt at triple junctions. The subscripts 'stress' and 'diffusion' denote the strain rate enhancement resulting from increasing the local stress and the rate of mass transfer, respectively. The term $\Delta d/d$ is a function of melt fraction as well as dihedral angle, reflecting the distribution topology of the melt phase, and has the form:

$$\frac{\Delta d}{d}=1.05f(\theta)\phi^{1/2} \tag{6}$$

where:

$$f(\theta)=\sin(30^\circ-(\theta/2))$$

$$\left(\frac{1+\cos\theta}{\sqrt{3}}-\sin\theta-\frac{\pi}{90}(30^\circ-(\theta/2))\right)^{-1/2} \tag{7}$$

Our experimental data for the diffusion creep regime are compared to the CK model in Fig. 10A, in which strain rate is plotted versus melt fraction. In this figure, our data deviate from the model at melt fractions greater than $\sim$0.05. As suggested by Hirth and Kohlstedt [14], the marked deviation of the experimental data from the CK model may be ascribed to the presence of melt along a significant number of the two-grain boundaries, which provides additional short circuit paths for diffusion. As stated above, the CK model is constrained by the condition that basaltic melt is present at three- and four-grain junctions in partially molten aggregates while two-grain boundaries remain melt-free. In reality, this situation applies only when the melt fraction is small ($\phi<0.01$). For the experiments with a larger amount of melt ($\phi>0.02$), a significant fraction of the grain boundaries are wetted by melt. In this case, the creep rate is not only enhanced by the presence of melt at triple junctions but also by the presence of melt along wetted grain boundaries. To take this difference into account, Hirth and Kohlstedt [14] modified the CK model to yield:

$$\dot{\varepsilon}(\phi)\propto\dot{\varepsilon}(0)\left(1-\frac{\Delta d}{d}\right)^{-2}_{\text{stress}}\left(\left(1-\frac{\Delta d}{d}\right)(1-\gamma\phi)\right)^{-2}_{\text{diffusion}} \tag{8}$$

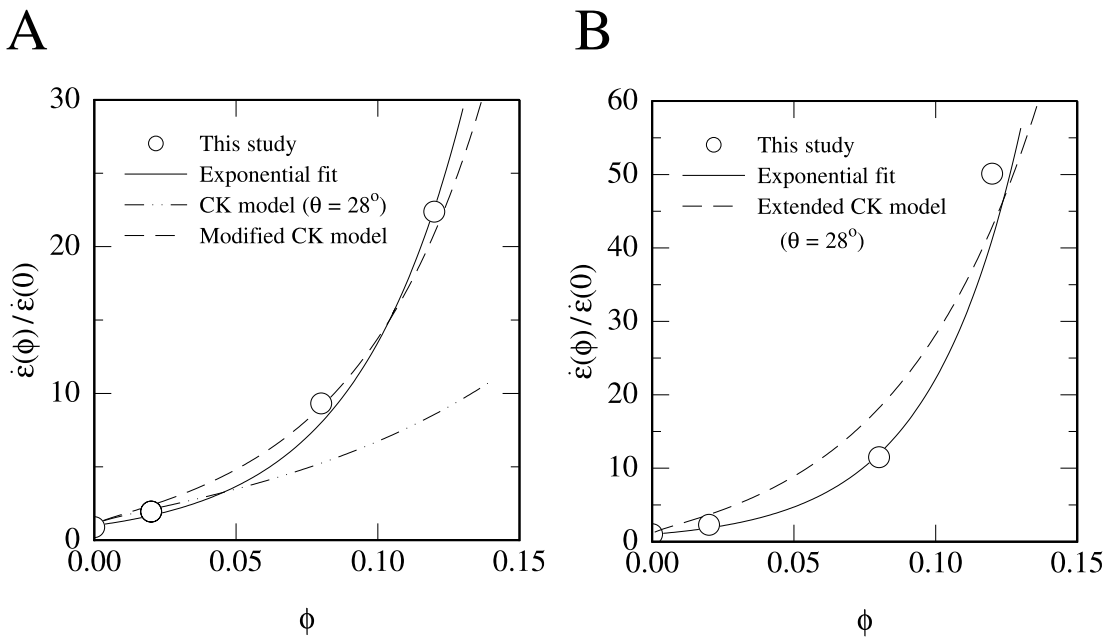

Fig. 10. Strain rate enhancement ($\dot{\varepsilon}(\phi)/\dot{\varepsilon}(0)$) versus melt fraction for deformation in (A) the diffusion creep regime and (B) the dislocation creep regime. Data points are the same as those used in Fig. 9. The solid lines in both (A) and (B) are fits to an exponential function, Eq. 4. The dashed lines are fits to (A) the modified CK model and (B) the extended CK model. In (A), the dot-dash line is a fit to the original CK model. Dihedral angle used in the CK model is 28°.

As illustrated in Fig. 10A, the modified model describes our data very well.

We have also applied the extended form of the CK model suggested by Hirth and Kohlstedt [15] to our dislocation creep results. In the dislocation creep regime, the enhancement in creep rate due to the presence of melt results mainly from the stress enhancement term in Eq. 5. That is, because melt occupies triple junctions, the local shear stress increases as the area of contact between neighboring grains decreases. In the dislocation creep regime, strain rate is proportional to stress to the nth power. Hence, with the presence of melt in triple junctions, the strain rate is enhanced as [15]:

$$\dot{\varepsilon}(\phi) \propto \dot{\varepsilon}(0)\left(1-\frac{\Delta d}{d}\right)^{-2n}_{\text{stress}} \tag{9}$$

Our dislocation creep data are compared to this extended model in Fig. 10B, in which strain rate is plotted versus melt fraction. Our data deviate slightly from the model. This deviation reflects, at least in part, the difference between the assumed and the actual melt distribution. Nonetheless, as a first-order estimate, in the dislocation creep regime the extended CK model describes our data fairly well.

It has been demonstrated that the influence of melt on creep rate can be described in two ways: empirically, our deformation data were fit with the exponential form given in Eq. 4 with different values for α in the diffusion and dislocation creep regimes; mechanistically, the cause of melt enhancement was analyzed with the modified and extended CK models to yield the very different forms stated in Eqs. 8 and 9 for the diffusion creep and dislocation creep regimes, respectively. Eqs. 8 and 9 can be rewritten into the forms given in Eqs. 10 and 11, respectively, for $\theta = 28°$ and, in the case of dislocation creep, $n = 3.5$:

$$\dot{\varepsilon}(\phi) \propto \dot{\varepsilon}(0)(1-1.19\phi^{1/2})^{-4}(1-3\phi)^{-2} \tag{10}$$

$$\dot{\varepsilon}(\phi) \propto \dot{\varepsilon}(0)(1-1.19\phi^{1/2})^{-7} \tag{11}$$

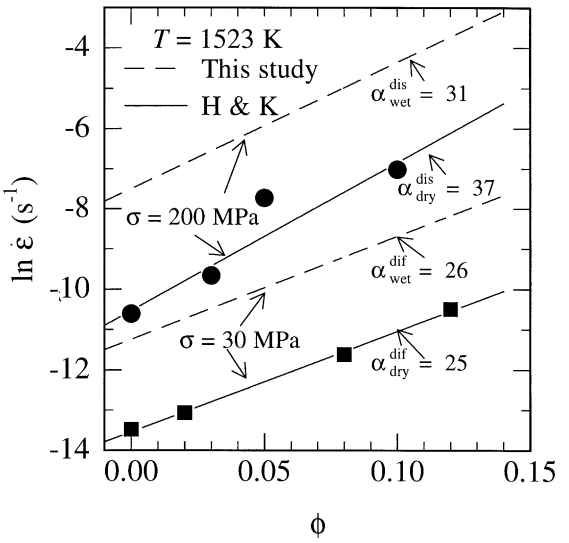

Fig. 11. Comparison of strain rate as a function of melt fraction for samples of olivine+basalt deformed in this study under hydrous conditions with results from Hirth and Kohlstedt [14,15] (H&K) obtained under anhydrous conditions. The dashed lines, which represent the data from this study, were taken from Fig. 9.

If ϕ is small ($\phi < 0.15$), Eqs. 10 and 11 can be approximated by exponential functions, thus possibly explaining why our data are reasonably well described empirically by Eq. 4.

4.2. Influence of water on the rheology of olivine–basalt aggregates

To evaluate the influence of water on the creep behavior of olivine–basalt aggregates, we compare our experimental results to related studies on (1) melt-added samples deformed under anhydrous conditions and (2) melt-free samples deformed under hydrous conditions. In Fig. 11, our experimental results for hydrous, melt-bearing samples are compared to the results of Hirth and Kohlstedt [14,15] for anhydrous, melt-bearing samples and to the results of Mei and Kohlstedt [9,10] for hydrous, melt-free samples. At the flow stresses and temperature given in Fig. 11, the ratio of creep rate for a sample deformed under water-saturated conditions (water fugacity ≈ 300 MPa) to the creep rate for a sample with the same melt fraction deformed under anhydrous conditions is a factor of ~ 10 in the diffusion creep regime and a factor of 10–20 in the dislocation creep regime. Under both hydrous and anhydrous conditions, the creep rate of olivine–basalt samples depends exponentially on melt fraction; hence, the flow law in both cases can be expressed in the form given by Eq. 4. For samples deformed under hydrous conditions, the flow law can be expressed as:

$$\dot{\varepsilon}(\phi,\ C_{\mathrm{OH}},\ \sigma,\ d,\ T,\ P) \approx \exp(\alpha_{\mathrm{wet}}\phi)\dot{\varepsilon}_{\mathrm{wet}}(C_{\mathrm{OH}},\ \sigma,\ d,\ T,\ P) \qquad (12a)$$

while for samples deformed under anhydrous conditions, the flow law is given by:

$$\dot{\varepsilon}(\phi,\ \sigma,\ d,\ T,\ P) \approx \exp(\alpha_{\mathrm{dry}}\phi)\dot{\varepsilon}_{\mathrm{dry}}(\sigma,\ d,\ T,\ P) \qquad (12b)$$

If measurement uncertainty is taken into account, the values of α_{wet} and α_{dry} are similar in both the diffusion creep regime and in the dislocation creep regime. That is, the influence of melt on the creep behavior of olivine–basalt aggregates is approximately the same under both hydrous and anhydrous conditions. This suggestion is not surprising if melt affects the creep rate primarily through physical processes such as enhancing local stress and matter transfer rate, since water makes little or no significant difference on melt morphology, as discussed above.

Table 2
Flow law parameters

Creep mechanism	A ($\mathrm{MPa}^{-(n+r)}$ $\mu\mathrm{m}^m$ s^{-1})	Q (kJ/mol)	V^* (10^{-6} m^3/mol)	m	n	r[a]	α
Diffusion	6.8×10^4	300 ± 30	20	3 ± 0.2	1 ± 0.1	1	26 ± 2
Dislocation	3.9×10^2	470 ± 50	20	0	3.5 ± 0.3	1	31 ± 4

[a] Based on Mei and Kohlstedt [9,10].

In Eq. 12a, the influence of water on the creep behavior of melt-free olivine aggregates has been determined by Mei and Kohlstedt [9,10]. Thus, Eq. 2 can be rewritten in the following form:

$$\dot{\varepsilon}(\sigma,\ d,\ \phi,\ C_{OH},\ T,\ P) = A\frac{\sigma^n}{d^m}\exp(\alpha\phi)f_{H_2O}^{r}\exp\left(-\frac{Q+PV^*}{RT}\right) \qquad (13)$$

Values for the parameters A, n, m, α, r, Q and V^* are summarized in Table 2 for both the diffusion and dislocation creep regimes. With the established relationship between water concentration and water fugacity [26], Eq. 13 can further be expressed in terms of water concentration and thus readily applied to water-under-saturated as well as water-saturated environments.

4.3. Geophysical applications

Experimental results in this study demonstrate that, in both the diffusion creep regime and the dislocation creep regime, the creep rate of olivine aggregates is influenced significantly by the presence of melt under hydrous conditions. These results provide constraints on the viscosity of Earth's mantle. Given reasonable estimates of water and melt conditions for the upper mantle, the viscosity in that geological region can be evaluated. Based on Eq. 13, the viscosity of regions of the upper mantle that differ not only in P and T but also in ϕ and f_{H_2O} (or C_{OH}) can be calculated. For example, the temperature–viscosity profiles developed by Hirth and Kohlstedt [1] for the region beneath a mid-ocean ridge can be compared with temperature–viscosity profiles in the mantle wedge above a subducting plate. The latter is expected to be more enriched in water and to have a higher melt concentration.

Based on the phase relationship for hydrous peridotitic and basaltic systems, Iwamori [4] modeled the transport of water and melt in subduction zones. His results yield water and melt contents as high as ~5 and ~18 wt%, respectively, along a subducting slab and in the overlying mantle wedge. This amount of water will saturate partially molten rocks in these regions. Based on Iwamori's data for a relatively cold slab subducting at an angle of 45°, we calculated a viscosity profile in a mantle wedge ~160 km away from the trench by taking both water and melt weakening effects into account. In Fig. 12, viscosity is computed based on the flow laws describing diffusion creep determined in this and previous studies [9]. In this illustration, the viscosity in the mantle wedge can vary ~3 orders of magnitude over a depth of ~60 km due to the combined effects of water and melt weakening. Pronounced minima in viscosity occur between 65 and 80 km and between 95 and 120 km, corresponding to maxima in both melt and water concentration. The associated increase in viscosity between 80 and 95 km reflects the decreases in the amount of melt and water predicted for this depth interval.

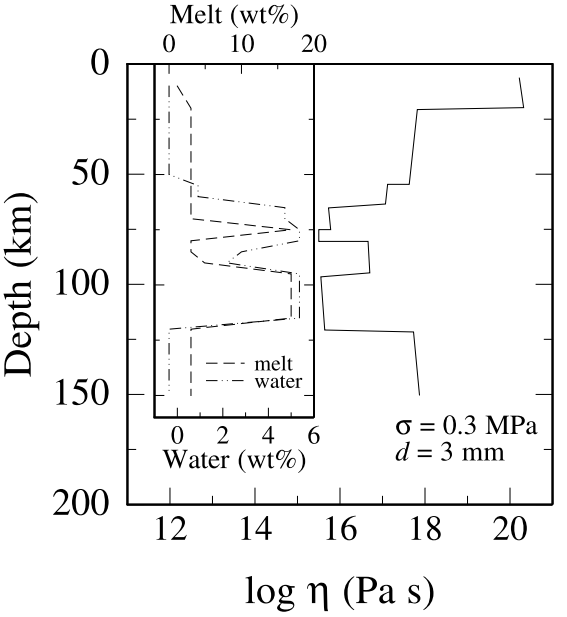

Fig. 12. Semi-log plot of viscosity profile for a mantle wedge 160 km from the trench for a relatively cold subducting slab. Viscosity is calculated with the flow law given in Eq. 13 using the information on water content and melt fraction from figure 5a of Iwamori [4], as summarized in the sub-plot included in the present figure. An adiabatic temperature profile with a potential temperature of 1525 K was used in the calculation.

As illustrated by this example for a mantle wedge above a subducting plate and the published viscosity profile for the region beneath a mid-

ocean ridge [1], the viscosity–depth profiles for specific regions of the Earth depend critically on the local concentration of melt and water. The constitutive equation reported in this paper provides a quantitative description of the dependence of viscosity on melt fraction and water concentration, as well as on pressure and temperature. Hence, it furnishes important constraints on the viscosity structure and geodynamical evolution of water-rich, partially molten regions of the upper mantle.

Acknowledgements

We wish to thank Greg Hirth, Steve Mackwell, Jan Tullis and Mark Zimmermann as well as an anonymous reviewer for providing very insightful and helpful comments during the review process. We are indebted to Steve Mackwell for suggesting the use of olivine single crystals embedded in a polycrystalline sample to quantify the water content of our samples. We especially acknowledge Mark Zimmermann for his involvement in carrying out the experiments and analyzing the results. We gratefully acknowledge the support of the National Science Foundation through Grants OCE-0002463, EAR-0126277, EAR-0079827, EAR-9906986 and INT-0123224.*[SK]*

References

[1] G. Hirth, D.L. Kohlstedt, Water in the oceanic upper mantle: implications for rheology, melt extraction and the evolution of the lithosphere, Earth Planet. Sci. Lett. 144 (1996) 93–108.

[2] A.V. Sobolev, M. Chaussidon, H_2O concentrations in primary melts from supra-subduction zones and mid-ocean ridges: implications for H_2O storage and recycling in the mantle, Earth Planet. Sci. Lett. 137 (1996) 45–55.

[3] D. McKenzie, The generation and compaction of partially molten rock, J. Petrol. 25 (1984) 713–765.

[4] H. Iwamori, Transportation of H_2O and melting in subduction zones, Earth Planet. Sci. Lett. 160 (1998) 65–80.

[5] N.L. Carter, H.G. Avé Lallemant, High-temperature flow of dunite and peridotite, Geol. Soc. Am. Bull. 81 (1970) 2181–2202.

[6] P.N. Chopra, M.S. Paterson, The role of water in the deformation of dunite, J. Geophys. Res. 89 (1984) 7861–7876.

[7] S.J. Mackwell, D.L. Kohlstedt, M.S. Paterson, The role of water in the deformation of olivine single crystals, J. Geophys. Res. 79 (1985) 11319–11333.

[8] S.I. Karato, M.S. Paterson, J.D. FitzGerald, Rheology of synthetic olivine aggregates: influence of grain size and water, J. Geophys. Res. 91 (1986) 8151–8176.

[9] S. Mei, D.L. Kohlstedt, Influence of water on plastic deformation of olivine aggregates: 1. Diffusion creep regime, J. Geophys. Res. 105 (2000) 21457–21469.

[10] S. Mei, D.L. Kohlstedt, Influence of water on plastic deformation of olivine aggregates: 2. Dislocation creep regime, J. Geophys. Res. 105 (2000) 21471–21481.

[11] R.F. Cooper, D.L. Kohlstedt, Rheology and structure of olivine–basalt partial melts, J. Geophys. Res. 91 (1986) 9315–9323.

[12] D.L. Kohlstedt, P.N. Chopra, Influence of basaltic melt on the creep of polycrystalline olivine under hydrous conditions, in: M.P. Ryan (Ed.), Magmatic Systems, Academic Press, San Diego, CA, 1994, pp. 37–53.

[13] Z.M. Jin, H.W. Green, Y. Zhou, Melt topology during dynamic partial melting of mantle peridotite, Nature 372 (1994) 164–167.

[14] G. Hirth, D.L. Kohlstedt, Experimental constraints on the dynamics of the partially molten upper mantle: Deformation in the diffusion creep regime, J. Geophys. Res. 100 (1995) 1981–2001.

[15] G. Hirth, D.L. Kohlstedt, Experimental constraints on the dynamics of the partially molten upper mantle: 2. Deformation in the dislocation creep regime, J. Geophys. Res. 100 (1995) 15441–15449.

[16] C.W. Burham, The importance of volatile constituents, in: J.S. Yoder (Ed.), The Evolution of the Igneous Rocks, Princeton University Press, Princeton, NJ, 1979, pp. 439–482.

[17] T.W. Sisson, T.L. Grove, Experimental investigations of the role of H_2O in calc-alkaline differentiation and subduction zone magmatism, Contrib. Mineral. Petrol. 113 (1993) 143–166.

[18] S.I. Karato, Does partial melting reduce the creep strength of the upper mantle?, Nature 319 (1986) 309–310.

[19] M.J. Daines, D.L. Kohlstedt, A laboratory study of melt migration, Phil. Trans. R. Soc. London 342(A) (1993) 43–52.

[20] M.S. Paterson, Rock deformation experimentation, in: A.G. Duba, W.B. Durham, J.W. Handin, H.F. Wang (Eds.), The Brittle–Ductile Transition in Rocks, AGU Monograph 56, 1990, pp. 187–194.

[21] M.S. Paterson, The determination of hydroxyl by infrared absorption in quartz silicate glasses and similar materials, Bull. Mineral. 105 (1982) 20–29.

[22] H.J. Frost, M.F. Ashby, Deformation-Mechanism Maps, Pergamon Press, Oxford, 1982, 166 pp.

[23] R.C. Gifkins, Optical Microscopy of Metals, Elsevier, New York, 1970.

[24] G.A. Gaetani, T.L. Grove, W.B. Bryan, The influence of water in the petrogenesis of subduction-related igneous rocks, Nature 365 (1993) 332–334.

[25] Q. Bai, D.L. Kohlstedt, Substantial hydrogen solubility in olivine and implication for water storage in the mantle, Nature 357 (1992) 672–674.
[26] D.L. Kohlstedt, H. Keppler, D.C. Rubie, Solubility of water in the α, β, and γ phases of $(Mg, Fe)_2SiO_4$, Contrib. Mineral. Petrol. 123 (1996) 345–357.
[27] E. Stolper, Water in silicate glasses: an infrared spectroscopic study, Contrib. Mineral. Petrol. 81 (1982) 1–17.
[28] M.J. Daines, F.M. Richter, An experimental method for directly determining the interconnectivity of melt in a partially molten system, Geophys. Res. Lett. 15 (1988) 1459–1462.
[29] E.B. Watson, Diffusion in fluid-bearing and slightly-melted rocks: experimental and numerical approaches illustrated by iron transport in dunite, Contrib. Mineral. Petrol. 107 (1991) 417–434.
[30] H. Jung, H.S. Waff, Olivine crystallographic control and anisotropic melt distribution in ultramafic partial melts, Geophys. Res. Lett. 25 (1998) 2901–2904.
[31] H.S. Waff, J.S. Bulau, Equilibrium fluid distribution in an ultramafic partial melt under hydrostatic stress conditions, J. Geophys. Res. 84 (1979) 6109–6114.
[32] G.N. Riley, D.L. Kohlstedt, The influence of H_2O and CO_2 on melt migration in two silicate liquid-olivine system, in: B. Evans, T.-F. Wong (Eds.), Fault Mechanism and Transport Properties of Rocks: A Festschrift in Honor of W.F. Brace, Academic Press, New York, 1992, pp. 281–294.
[33] P.B. Kelemen, G. Hirth, N. Shimizu, M. Spiegelman, H.J.B. Dick, A review of melt migration processes in the adiabatically upwelling mantle beneath oceanic spreading ridges, Phil. Trans. R. Soc. London 355 (1997) 283–318.
[34] R.F. Cooper, D.L. Kohlstedt, Solution-precipitation enhanced diffusional creep of partially molten olivine basalt aggregates during hot-pressing, Tectonophysics 107 (1984) 207–233.
[35] R.F. Cooper, D.L. Kohlstedt, K. Chyung, Solution-precipitation enhanced creep in solid-liquid aggregates which displays a non-zero dihedral angle, Acta Metall. 37 (1989) 1759–1771.
[36] R.L. Coble, A model for boundary diffusion controlled creep in polycrystalline materials, J. Appl. Phys. 34 (1963) 1679–1682.